Electronic Supplementary Material (ESI) for Energy & Environmental Science.
This journal is © The Royal Society of Chemistry 2021

Supporting Information

Reaction intermediates-mediated electrocatalysts synthesis favors specified facets and defects exposure for efficient nitrate-ammonia conversion

Qi Hu[a], Yongjie Qin[a], Xiaodeng Wang[a], Ziyu Wang[a], Xiaowan Huang[a], Hongju Zheng[a], Keru Gao[a], Hengpan Yang[a], Peixin Zhang[a], Minhua Shao[b] and Chuanxin He[a]*

[a]College of Chemistry Environmental Engineering, Shenzhen University, Shenzhen, Guangdong, 518060, People's Republic of China

[b] Department of Chemical and Biological Engineering and Energy Institute, The Hong Kong University of Science and Technology, Kowloon, Hong Kong, China.

Experiment section

Synthesis of CuO-NBs-111

Ultrathin CuO nanobelts with abundant CuO(111) facets (denoted CuO-NBs-111) were synthesized by a modified hydrothermal method based on the literature[1]. In a typical process, 32 mg $CuSO_4 \cdot 5H_2O$ was dissolved into 2 mL deionized water, and then 0.8 mL 1 M KOH aqueous solution and 0.3 mL 15% $NH_3 \cdot H_2O$ were separately added drop by drop to the above solution under vigorous stirring at room temperature via a syringe pump for five minutes. The obtained blue suspension was then heat to 80 ^oC and maintained for 12 hours. Finally, the black product was obtained through centrifugation, and then dried overnight at 60 °C in the vacuum oven.

Synthesis of Cu-NBs-100, Cu-NBs-111 and Cu-NPs-111

Cu nanobelts rich in (100) facets (denoted Cu-NBs-100) were synthesized via an electrochemical reduction of CuO-NBs-111 under conditions similar to NO_3^-RR, which operated at a reduction potential of -0.4 V vs RHE in the electrolyte of 1 M KOH containing 0.5 M NO_3^- for more than 1 h. For comparison, the Cu nanobelts dominated with (111) facets (denoted Cu-NBs-111) were also prepared by using the similar electrochemical reduction method as Cu-NBs-100 but without addition of NO_3^-. To investigate the influence of ultrathin nanobelts structures on electrochemical performance, we also synthesized Cu nanoparticles dominated with (111) facets (Cu-NPs-111) using sodium borohydride as reductants. In details, 300 mg $Cu(NO_3)_2 \cdot 3H_2O$ was dissolved into 10 mL deionized water to obtain a blue solution, and next 150 mg $NaBH_4$ was added into the blue solution under vigorous stirring for 10 minutes. The resulting products were washed in deionized water for three times, collected by centrifugation and dried at 60 °C for 12 h in a vacuum oven.

Material characterizations

The morphologies of all samples were investigated on transmission electron microscope (TEM) and high-resolution transmission electron microscopy (HRTEM)

(JEM-2100F). The thickness of nanobelts was determined by using atomic force microscope (AFM, MultiMode 8, Bruker). X-ray diffraction (XRD) patterns were measured on a high-power X-ray diffractometer (Rigaku Mini Flex 600) using Cu Kα radiation (λ = 0.15418 nm). X-ray photoelectron spectroscopy (XPS) tests were performed on an X-ray photoelectron spectrometer (Thermo VG Scientific ESCALAB 250, Thermo Electron, U.K.). FT-IR was measured on a Fourier transform infrared spectrometer (IR Affinity-1). UV-Vis tests were carried out via an Ultraviolet–Visible Spectrophotometer (UV-2550).

Electrochemical Measurements

All electrochemical tests were carried on a H-type electrochemical cell by using an electrochemical station (CHI 760E, CH Instrument Inc) at room temperature. The NO_3^-RR performance was first evaluated in an alkaline electrolyte (i.e., 1 M KOH aqueous solution with 0.1 M NO_3^-). A three-electrode system was constructed to accomplish the tests: Hg/HgO (in 1 M KOH) and Pt foil were employed as the reference and the counter electrode, respectively, and a piece of carbon paper (0.25 cm^2) with electrocatalysts (mass loadings of 1 mg cm^{-2}) served as the working electrode. The electrocatalyst inks were prepared by well dispersing a specific electrocatalyst in a mixed solution ($V_{ethanol}$: V_{Nafion} = 92 : 8) under ultrasonic conditions. The H-type cell was separated by a piece of FAB-PK-130 anion exchange membrane. To eliminate the impacts of air, Ar gas was uninterruptedly pumped into the cathodic side of the H-type cell. When the alkaline electrolyte changed to the neutral (i.e., 0.1 M phosphate buffer solution (PBS) with 500 ppm NO_3^-), the reference electrode was change to saturated calomel electrode, and the separator was changed to Nafion 117 ionic exchange membrane. And, the Pt foil was employed as the counter electrode. All tested potentials were converted into the reversible hydrogen electrode (RHE) based on the Nernst equation: $E_{RHE} = E_{Hg/HgO} + 0.098 + 0.0591pH$ (pH =14), $E_{RHE} = E_{SCE} + 0.242 + 0.0591pH$ (pH =7). iR compensation were performed before recording all LSV, where R is the solution resistance. All LSV curves were recorded at a scan rate of 5 mV s^{-1}. EIS measurements were performed

from 1 MHz to 1 Hz. According to our previous literatures, the ECSA values were evaluated via the measurements of cyclic voltammetry (CV) over a potential range free of Faradic current densities.[2]

Cyclic voltammetry (CV) in Ar-saturated 1 M KOH was adopted to test the electro-adsorption of hydroxide on different electrocatalysts. In order to maximumly avoid the oxidation of Cu, a potential range from -0.2 to 0.55 V vs RHE was selected.

^{1}H NMR was used to perform isotope tracing experiments on a H-nuclear magnetic resonance (H-NMR) technic (Bruker AVANCE III 600 MHz). As for the quantifying the content of NH_3 in liquid products through the ^{1}H NMR, maleic acid (MA) was used an internal standard. Gas products were analyzed by using Gas Chromatography (Shanghai Fuli GC9790-Plus).

Ammonia detection and efficiency calculations

The concentration of NH_3 in liquid products was determined via an indophenol blue method.[3] To make the NH_3 concentration well situate at the linear range of this method, the liquid products obtained for 3600 s continuous electrolysis were diluted by deionized water in advance. Then, a mixed solution composed of salicylic acid (0.036 mol), potassium sodium tartrate tetrahydrate (0.018 mol), and NaOH (0.036 mol) dissolved in 100 ml deionized water was prepared and served as coloring agents. Afterwards, 500 μL of coloring agents were added into 4 ml of diluted liquid products, followed by adding 50 μL NaClO (available chlorine 6-14%), and 50 μL NaOH solution (0.75 M). The resulting solution was rested for 1 h. Finally, the concentration of NH_3 was quantified by the absorbance peak at a wavelength ~655 nm. The Faradaic efficiency toward NH_3 (FE_{NH3}) was determined based on the following equation:

$$\text{Faradaic efficiency} = \frac{nV_{catholyte}C_{NH3}F}{Q}$$

where n stands for the number of transferred electrons for the formation of 1 mol of ammonia, here is 8; $V_{catholyte}$ is the volume of liquid product (L), and the value is 0.025 L; C_{NH3} is the detected concentration of ammonia (M) detected; F is the Faraday constant (96485 C·mol^{-1}); Q represents the total consumed charge (Q = it).

NO_2^- and N_2H_4 detection

The NO_2^- and N_2H_4 in liquid products were detected according to the method of Griess[4] and Watt & Chrisp[4] method. In the Griess method, the coloring agents were prepared by dissolving H_3PO_4 (2.94 mL), N-(1-naphthyl)ethyldiamine dihydrochloride (0.1 g), and sulfonamide (1.0 g) in deionized H_2O (50 ml). In a typical process, the coloring agent (2.0 ml) was added into the liquid product (2.0 ml), and the mixed solution was allowed to stand at room temperature for 15 min to generate a magenta azodye. Finally, the concentration of NO_2^- was determined by the peak at ~540 nm on UV-Vis Spectroscopy.

In the case of N_2H_4 detection, the coloring agent was prepared by dissolving 5.99 g of p-(dimethylamino) benzaldehyde in a mixed solution of concentrated hydrochloric acid (30 mL) and absolute ethanol (300 mL). Then, obtained liquid products were mixed with 0.5 ml coloring agent, and the resulting solution was rested for 5 min. Finally, the concentration of N_2H_4 was determined by the absorbance peak at 460 nm on UV-Vis Spectroscopy.

Computational Details

We performed first principles density functional theory (DFT) calculations using the Vienna ab initio Simulation Program (VASP) package.[5] The method of projector-augmented wave (PAW) was utilized to decouple the core from valence electrons.[6] The exchange-correlational effects of valence electrons were described through the method of generalized gradient approximation (GGA) with a Perdew−Burk−Ernzerhof (PBE) functional.[6] A cutoff energy of 400 eV was offered and a Monkhorst–Pack k-point sampling (3×3×1) were employed. The model was optimized to converge the absolute energy to 1×10^{-4} eV with a force convergence of 0.02 eV/Å. Furthermore, all calculations were spin polarized, and the DFT-D3 Grimme method was applied to describe the weak van der Waals interaction. According to literatures, four layers of Cu(100) surfaces containing 36 Cu atoms and

the defective Cu(100) surfaces containing 35 Cu atoms were chosen as structural models to compute the performance for NO_3^-RR.[7] The adjacent slabs were separated by a vacuum layer in thickness of 15 Å along the z-direction. Given that the electrons were participated in the entire processes of electrocatalytic reactions, the standard hydrogen electrode model was adopted.

The free energy change (ΔG) in an elementary reaction was calculated by $\Delta G=\Delta E+\Delta ZPE-T\Delta S$, where the ΔE, ΔZPE, and TΔS represent the difference of total energy, zero-point energy, and entropy between the initial state and final states, respectively. T is the reaction temperature (298.15 K). As for the NO_3^- adsorption, the overall Gibbs free energy from the solution phase was calculated based on previous literatures.[8]

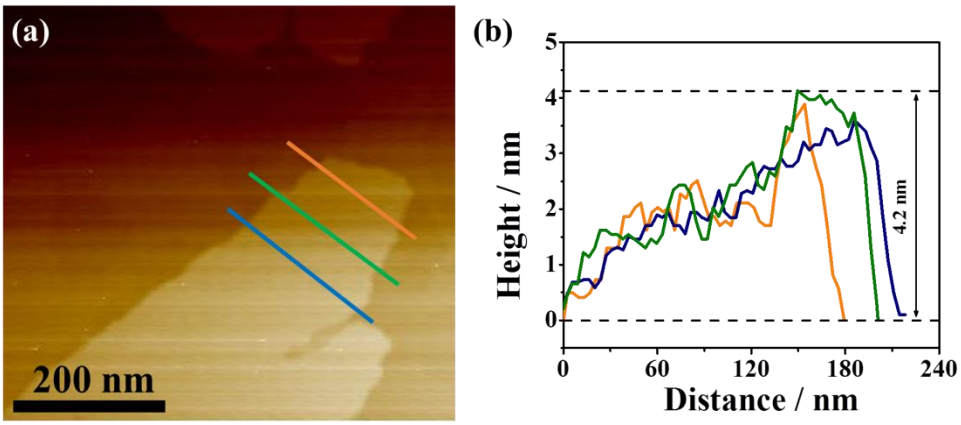

Figure S1 (a) AFM images of CuO-NBs-111, and (b) thickness of CuO nanobelts.

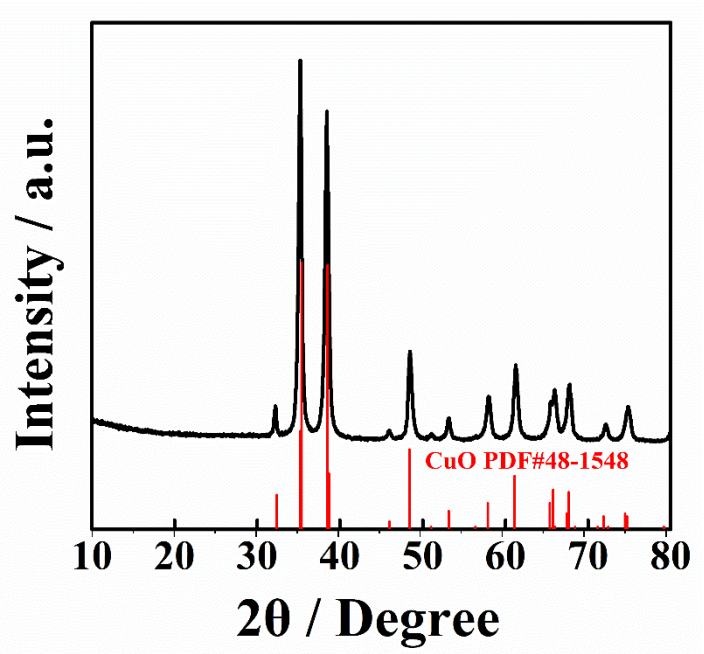

Figure S2 XRD patterns of CuO-NBs-111 precursors, which were synthesized via a hydrothermal method.

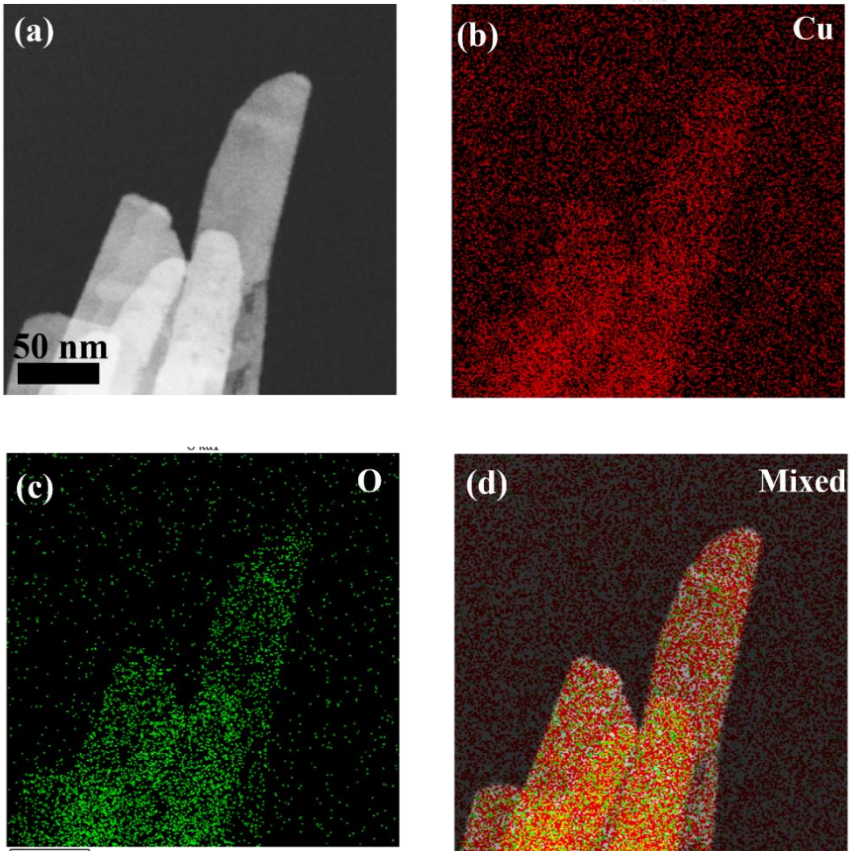

Figure S3 (a) HADDF-STEM images of CuO-NBs-111 with EDX mapping of (b) Cu, (c) O, and (d) mixed Cu and O elements.

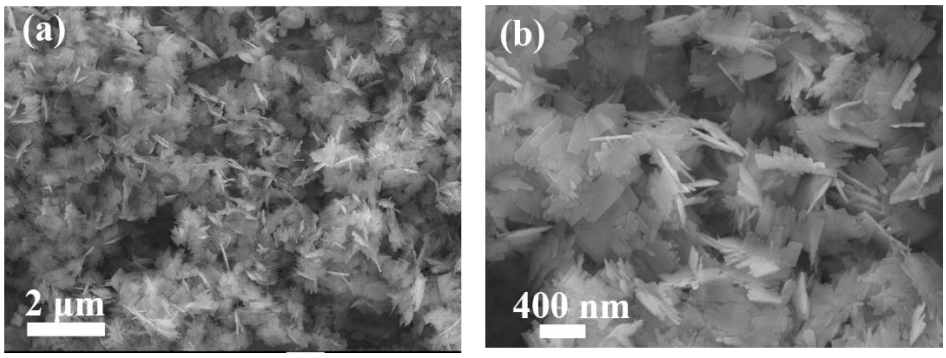

Figure S4 SEM images of Cu-NBs-100.

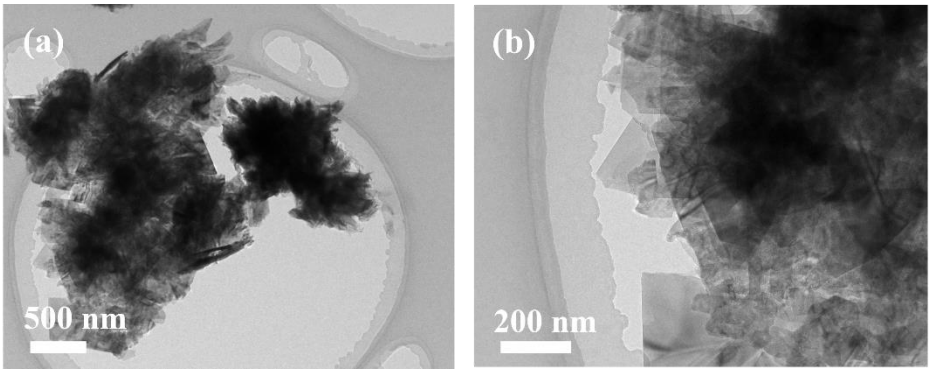

Figure S5 TEM images of Cu-NBs-100.

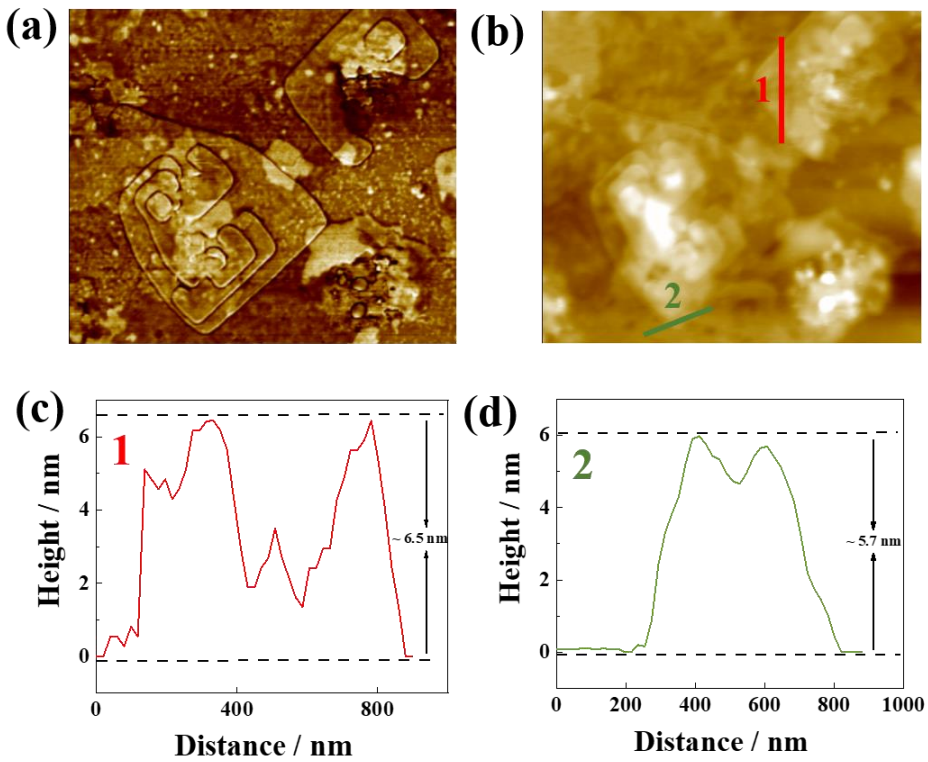

Figure S6 (a, b) AFM images of Cu-NBs-100. Thickness of nanobelts based on (c) line 1 and (d) line 2.

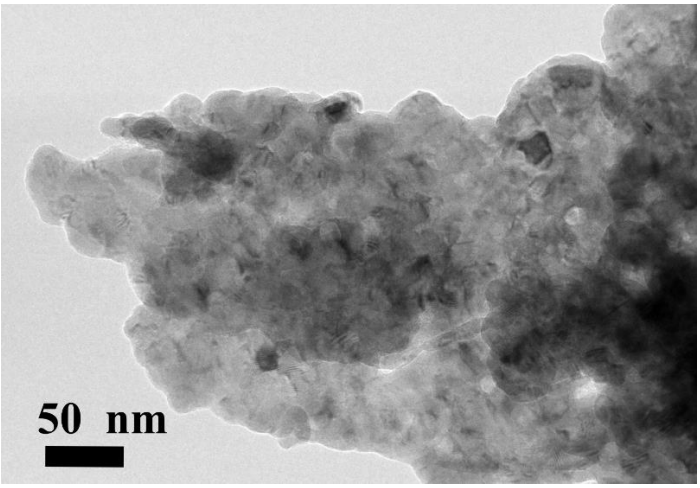

Figure S7 TEM images Cu-NBs-100, which were synthesized through the electrochemical reduction of CuO-NBs-111 under NO_3^-RR conditions.

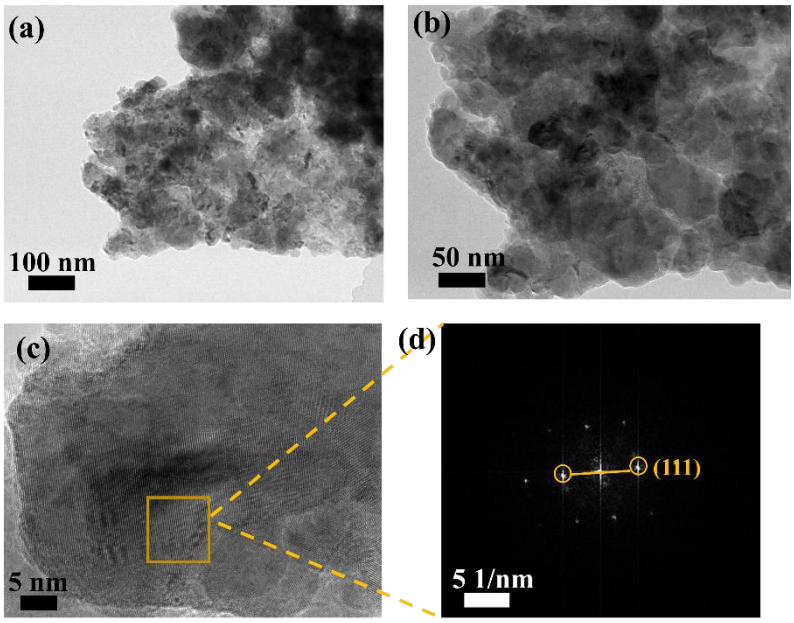

Figure S8 (a, b) TEM and (c) HRTEM images of Cu-NBs-111, (d) displayed FFT of Cu phase in (c).

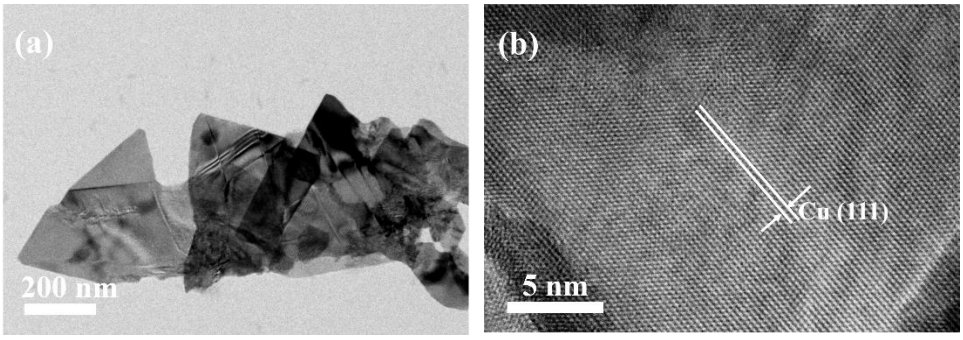

Figure S9 (a) TEM and (b) HRTEM images of CuO-NBs-111 after the electrochemical reduction at the potential of -0.4 V vs RHE in the electrolyte of 1 M KOH with 0.1 M NO_3^- for 1 h.

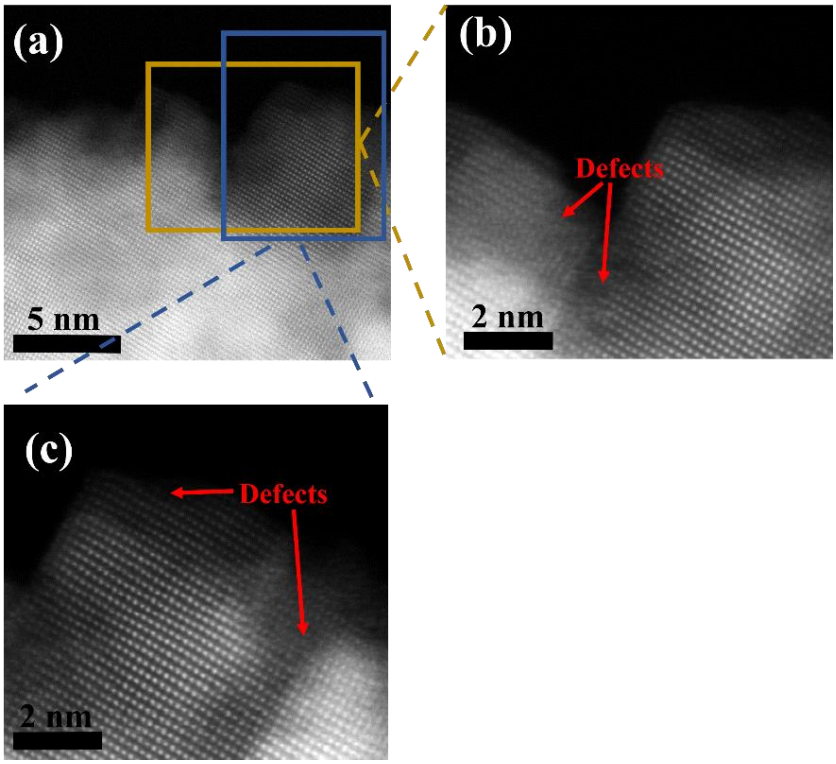

Figure S10 (a) HADDF-STEM images of Cu-NBs-100. (b, c) Partial enlarged images of (a).

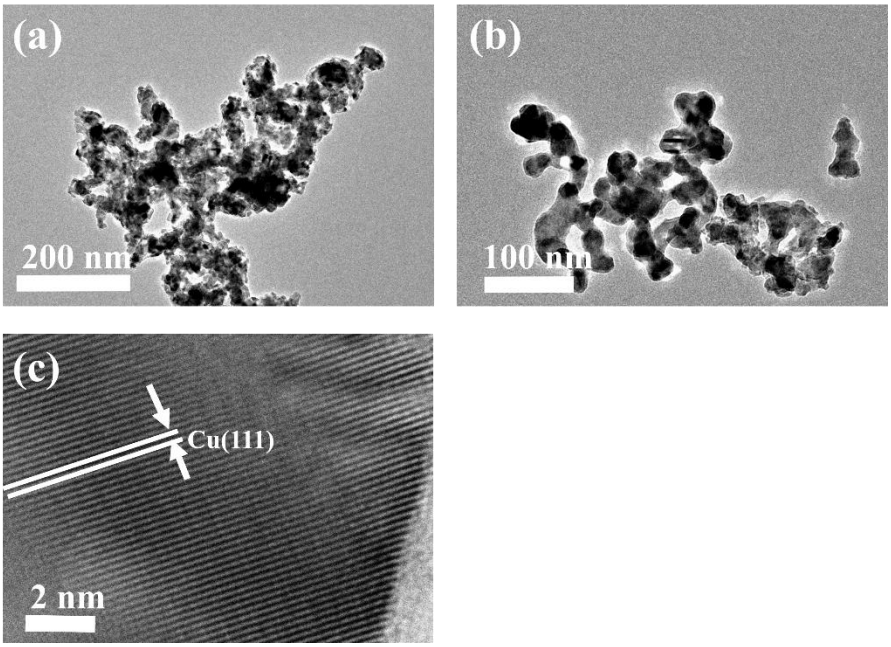

Figure S11 (a, b) TEM and (c) HRTEM images of Cu-NPs-111, which is dominated with (111) facets.

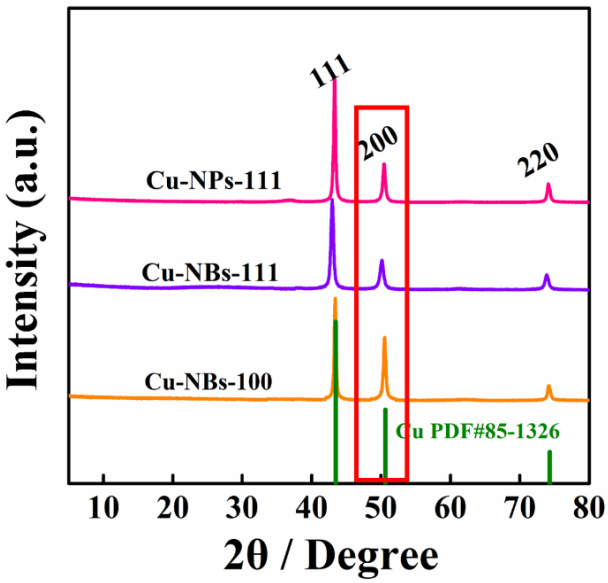

Figure S12 XRD patterns of Cu-NBs-100, Cu-NBs-111, and Cu-NPs-111. (100, and 111 represent the surface exposed facet of Cu)

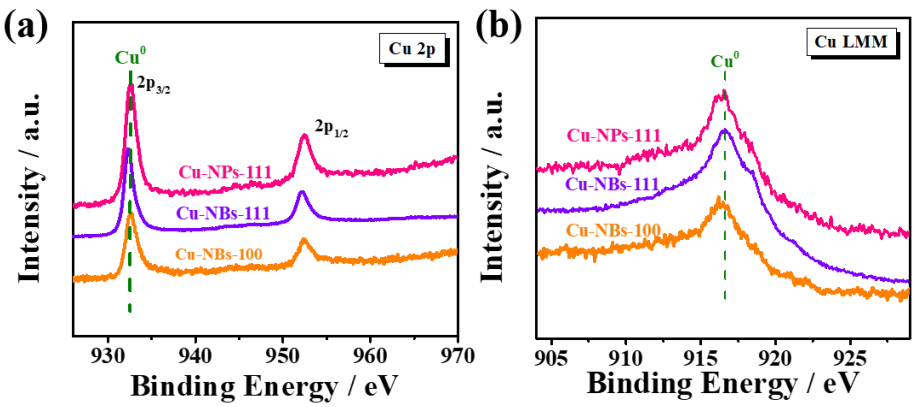

Figure S13 XPS spectra of (a) Cu 2p and (b) Cu LMM of Cu-NBs-100, Cu-NBs-111, and Cu-NPs-111.

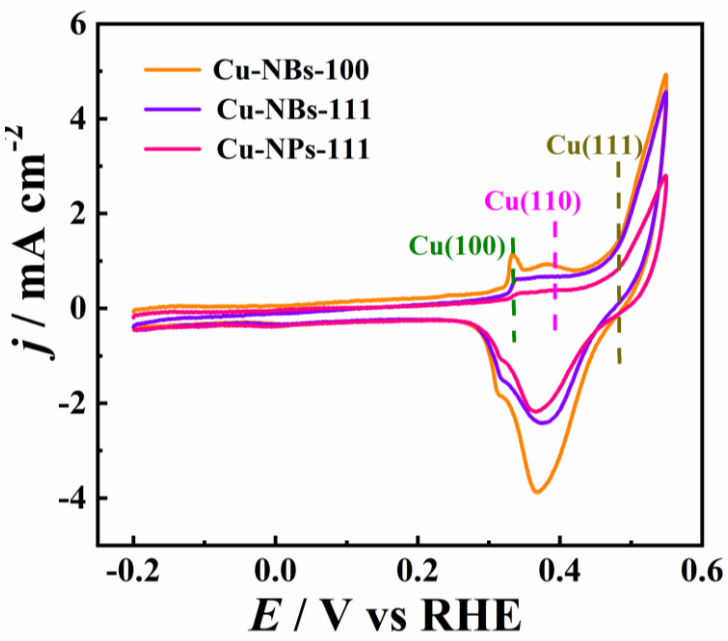

Figure S14 OH^- adsorption peaks of Cu-NBs-100, Cu-NBs-111, and Cu-NPs-111 obtained by voltammograms in Ar-saturated 1 M KOH.

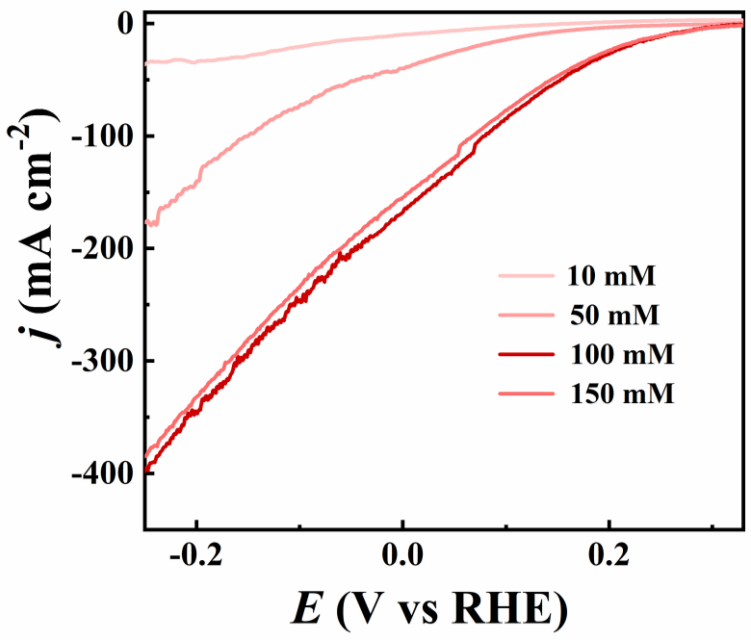

Figure S15 LSV of Cu-NBs-100 for NO_3^-RR in 1 M KOH with different NO_3^- concentration.

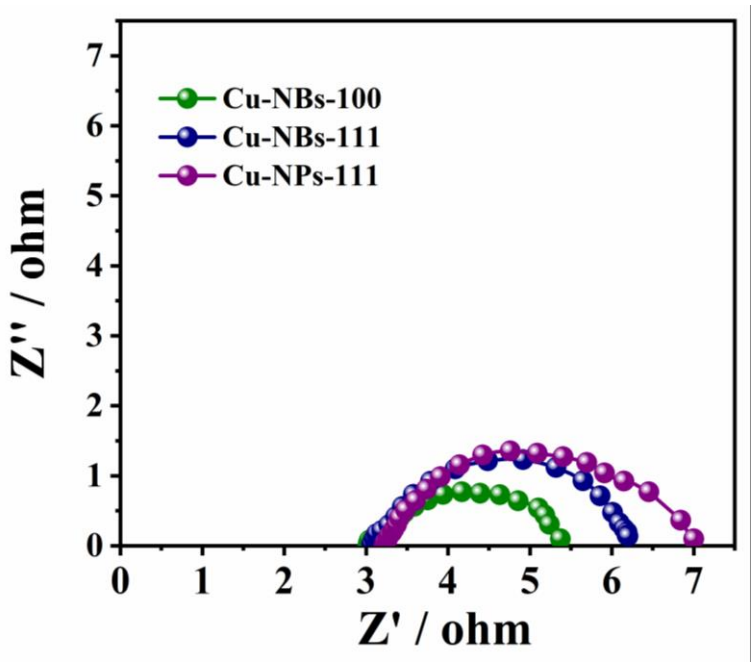

Figure S16 ESI measurements of Cu-NBs-100, Cu-NBs-111, and Cu-NPs-111 at the potential of -0.15 V vs RHE.

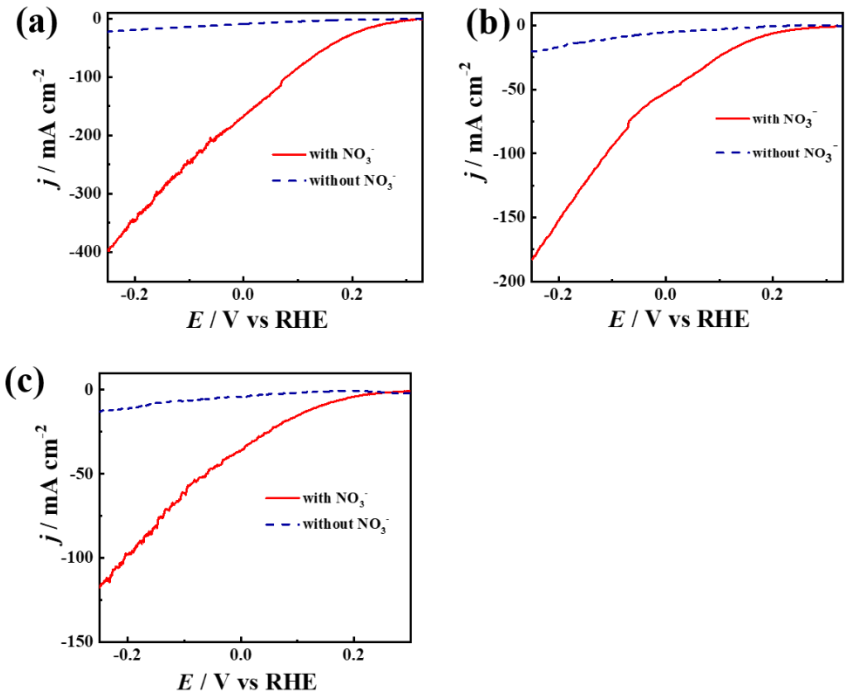

Figure S17 LSV of (a) Cu-NBs-100, (b) Cu-NBs-111, and (c) Cu-NPs-111 in the media of KOH with and without 0.1 M NO_3^-

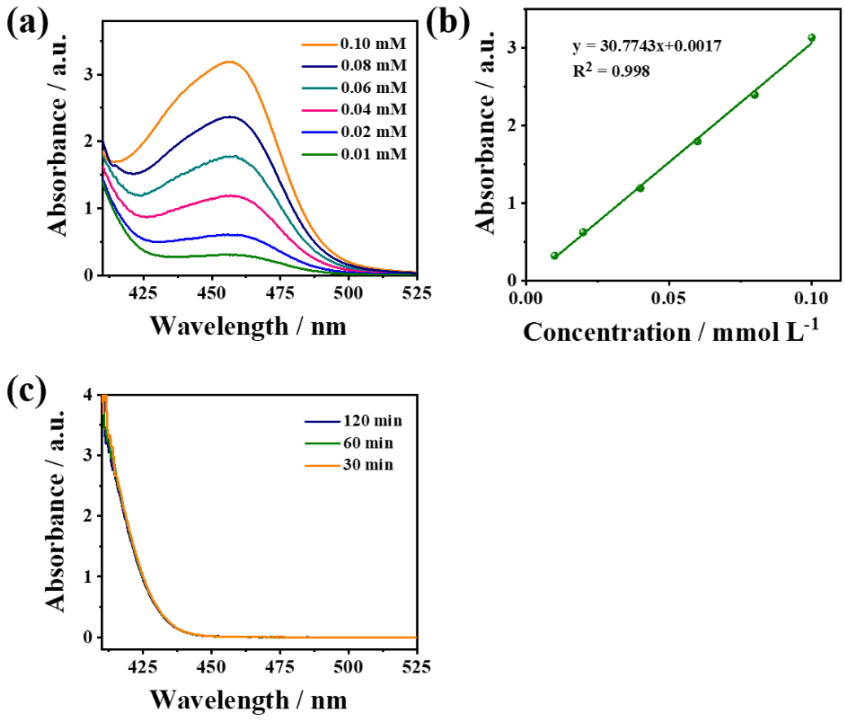

Figure S18 Quantifying produced hydrazine hydrate (N_2H_4) in the electrolyte using the Watt & Chrisp method. (a) UV-Vis adsorption spectra of standard solution containing different concentration of N_2H_4. (b) The linear standard plot to determine N_2H_4 yields. (c) Representative UV-Vis adsorption spectra of different-time NO_3^-RR electrolyte obtained on the Cu-NBs-100 for different-time NO_3^-RR after the addition of coloring agent.

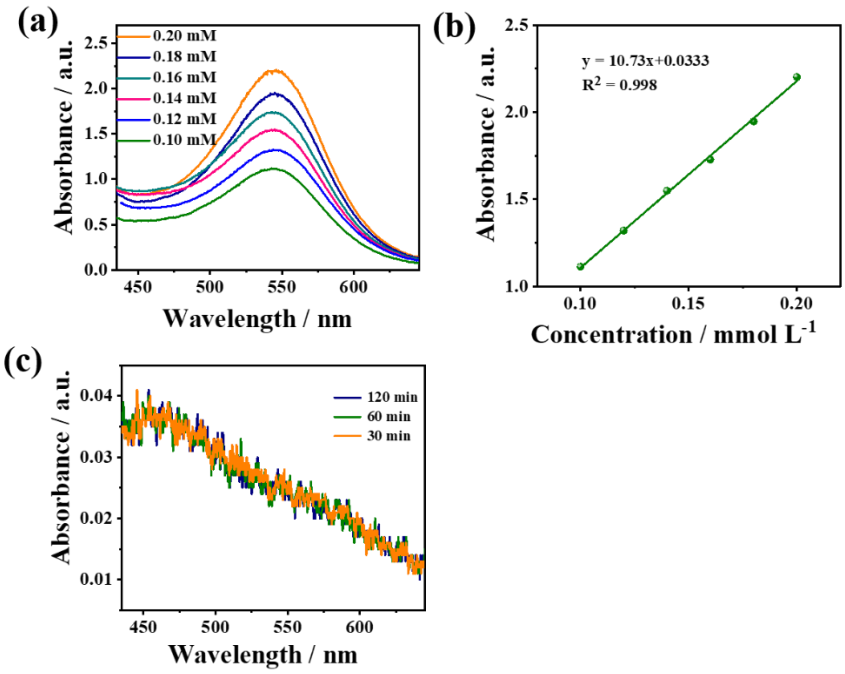

Figure S19 Quantifying produced nitrite (NO_2^-) in the electrolyte using the Griess method. (a) UV-Vis adsorption spectra of standard solution containing different concentration of NO_2^-. (b) The linear standard plot to determine NO_2^- yields. (c) Representative UV-Vis adsorption spectra of different-time NO_3^-RR electrolyte obtained on the Cu-NBs-100 after the addition of coloring agent.

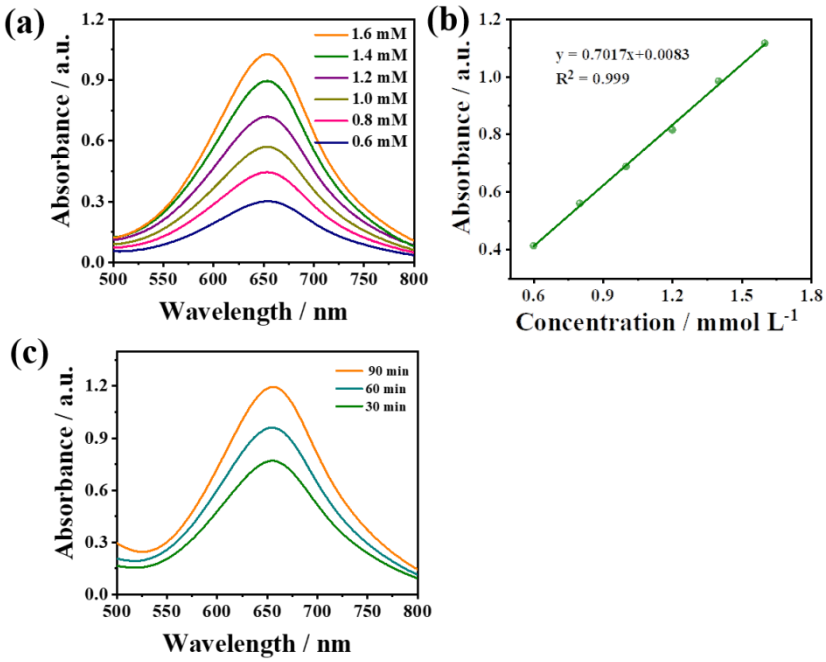

Figure S20 Quantifying produced ammonia (NH_3) in the electrolyte using the indophenol blue method. (a) UV-Vis adsorption spectra of standard solution containing different concentration of NH_3. (b) The linear standard plot to determine NH_3 yields. (c) Representative UV-Vis adsorption spectra of different-time NO_3^-RR electrolyte obtained on the Cu-NBs-100 after the addition of coloring agent.

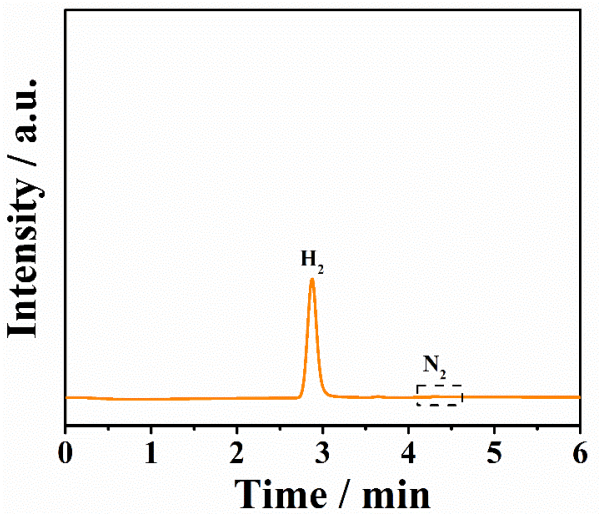

Figure S21 Representative gas-chromatography of gas products obtained on the Cu-NBs-100.

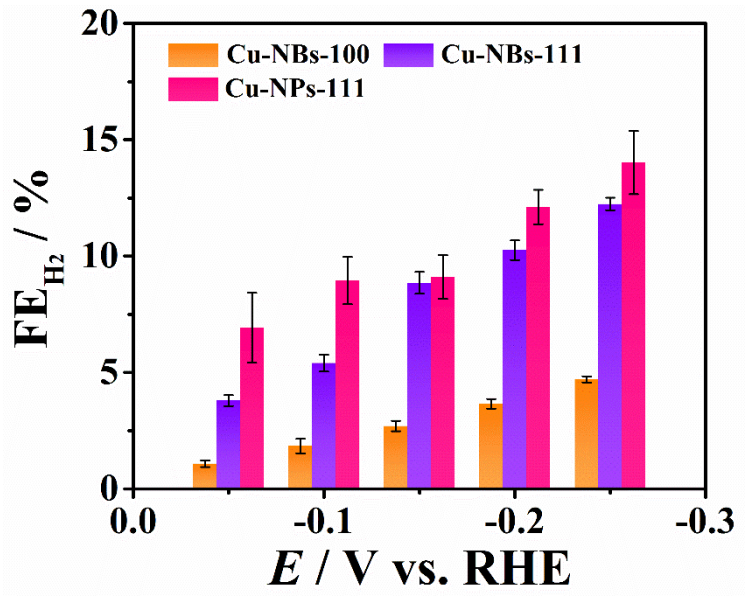

Figure S22 FE_{H2} of Cu-NBs-100 for NO_3^-RR at the potential range from -0.05 to -0.25 V vs RHE in 1 M KOH containing 0.1 M NO_3^-.

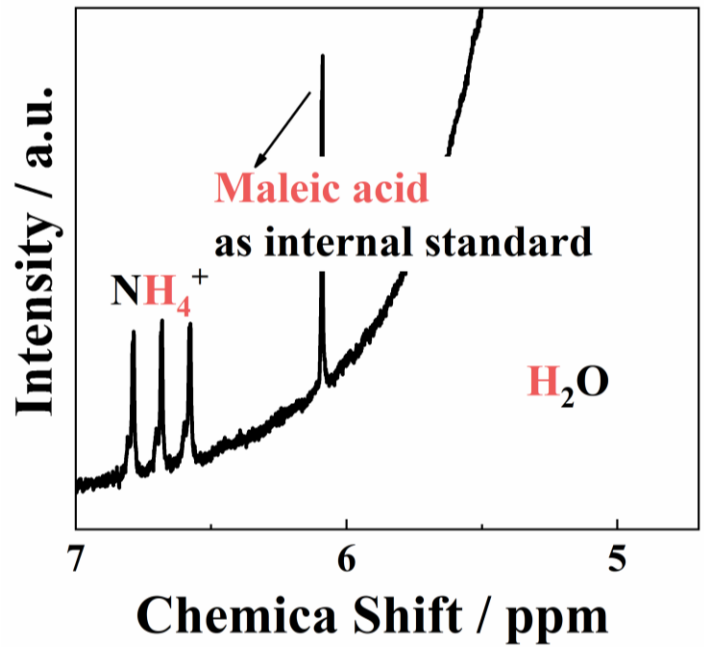

Figure S23 ^{1}H NMR spectra of liquid products obtained on the Cu-NBs-100 from NO_3^-RR at the potential of -0.15 V vs RHE for 1 h.

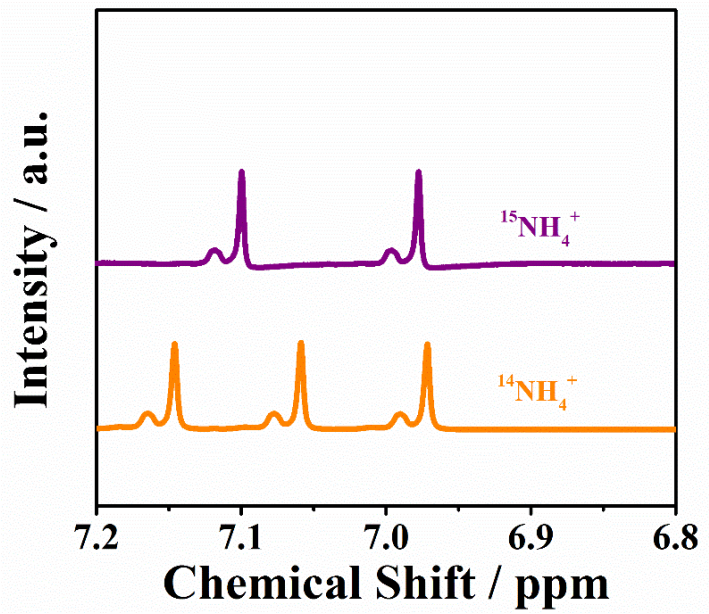

Figure S24 ^{1}H NMR spectra of liquid products obtained through NO_3^-RR of ^{14}N nitrate and ^{15}N nitrate.

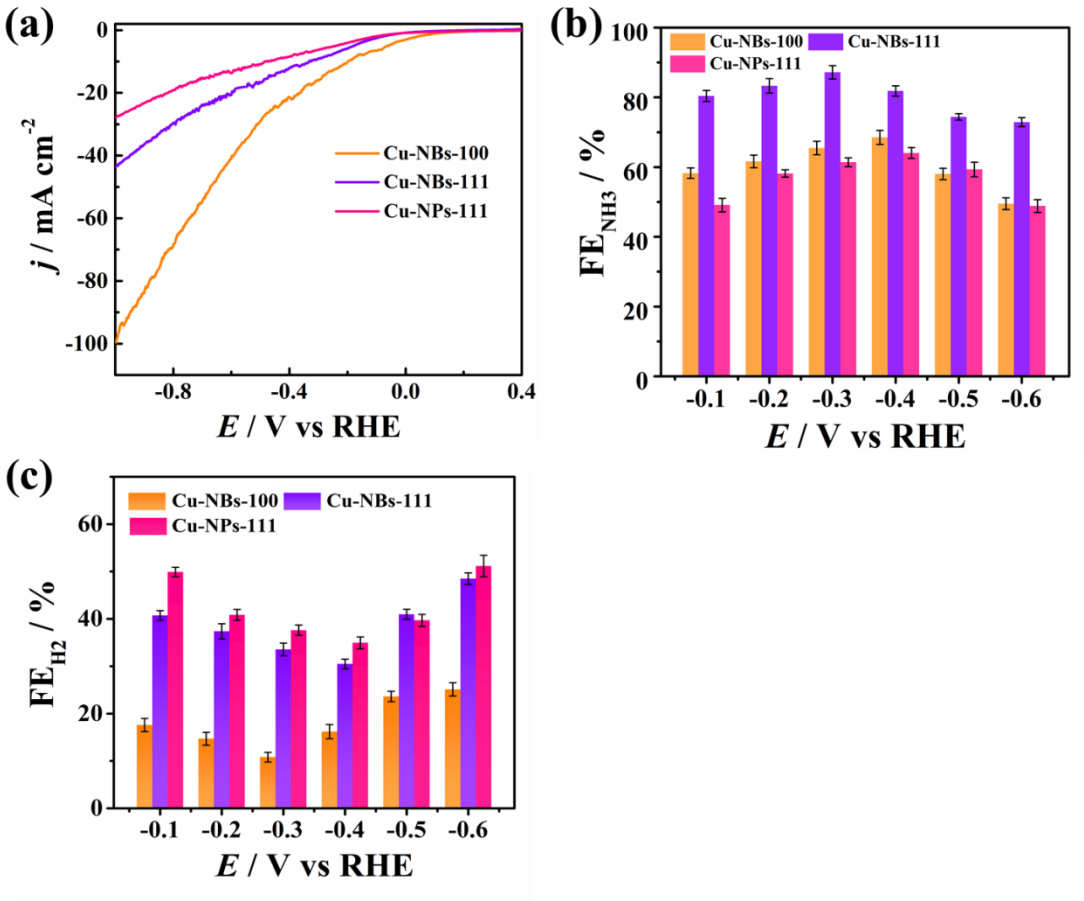

Figure S25 (a) LSV, (b) FE_{NH3}, and (c) FE_{H2} of Cu-NBs-100, Cu-NBs-111, and Cu-NPs-111 for NO_3^-RR in 0.1 M PBS with 500 ppm NO_3^-.

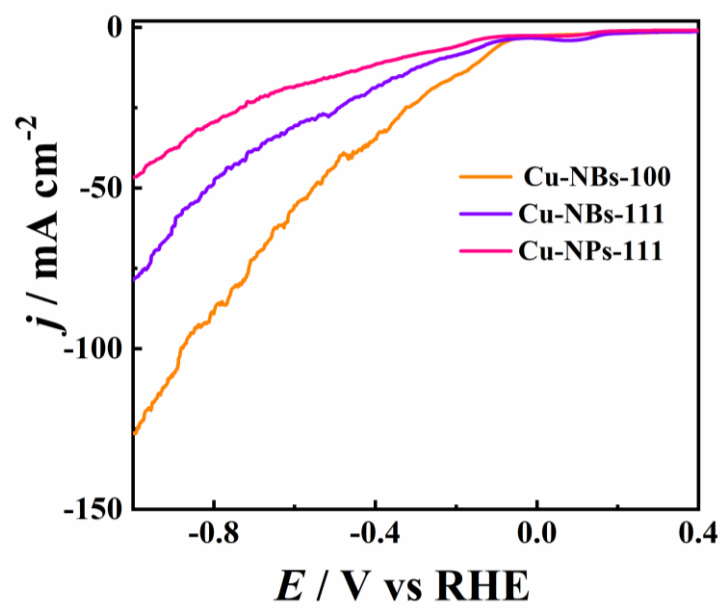

Figure S26 LSV of Cu-NBs-100, Cu-NBs-111, and Cu-NPs-111 for the NO_3^-RR in 1 M PBS solution with 500 ppm NO_3^-.

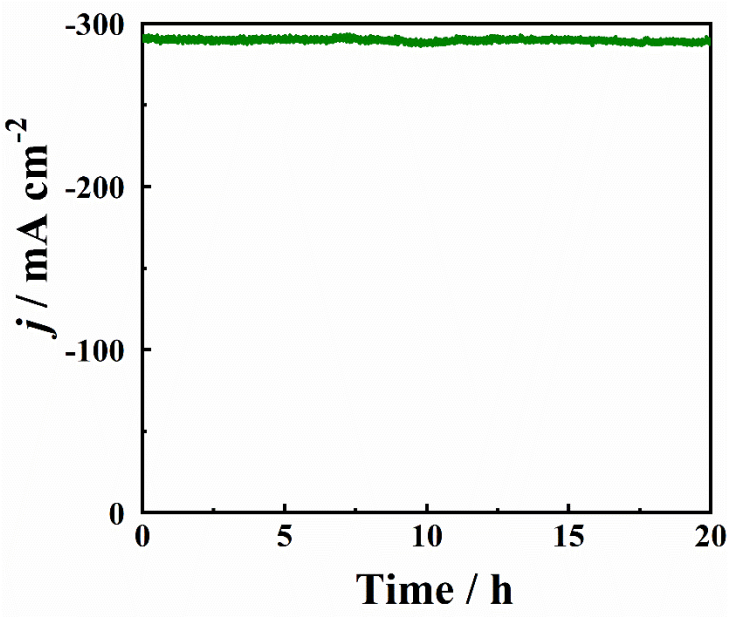

Figure S27 Stability test of Cu-NBs-100 at the potential of -0.15 V vs RHE for 20 h in 1 M KOH containing 0.1 M NO_3^-.

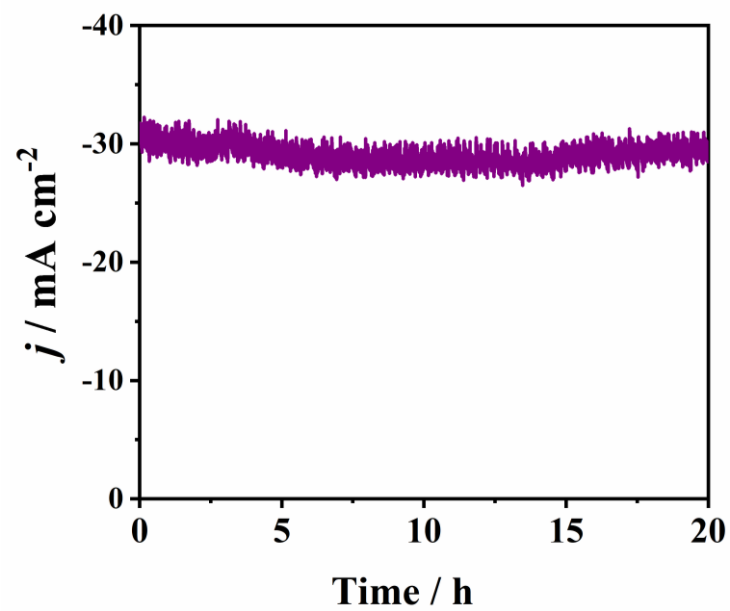

Figure S28 Stability test of Cu-NBs-100 in 0.1 M PBS with 500 ppm NO_3^- at the potential of -0.5 V vs RHE for 20 h.

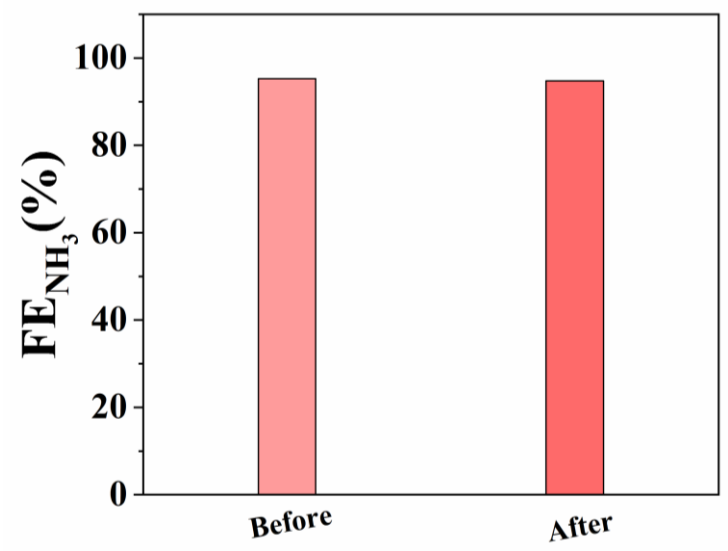

Figure S29 FE_{NH3} of Cu-NBs-100 at the potential of -0.15 V vs RHE in 1 M KOH with 0.1 M NO_3^- before and after the 20 h stability test.

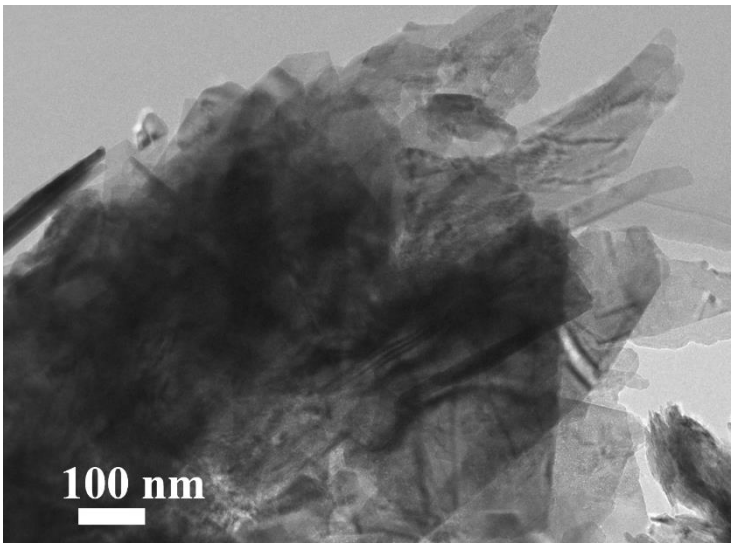

Figure S30 TEM images of Cu-NBs-100 after the 20 h stability test.

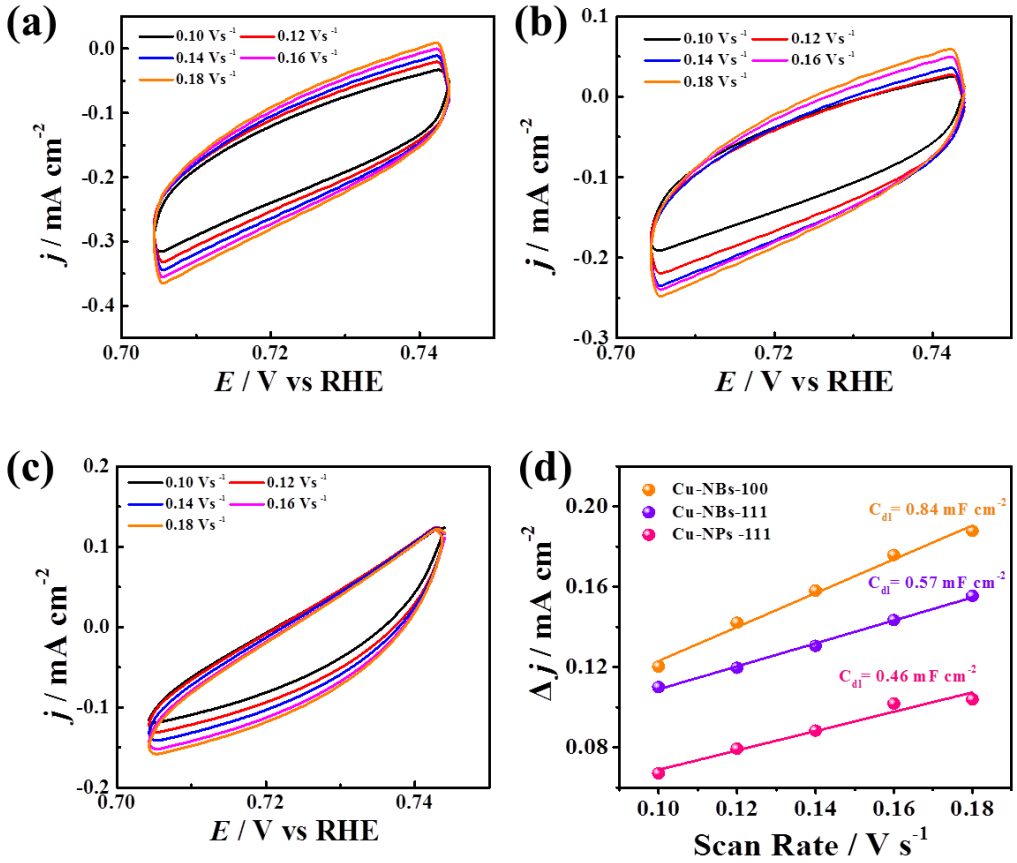

Figure S31 CV of (a) Cu-NBs-100, (b) Cu-NBs-111, and (c) Cu-NPs-111 at different scan rates over a potential range that free of Faradic current densities. (d) Profiles of capacitance Δj ($|j_{charge}-j_{discharge}|$) as a function of scan rates.

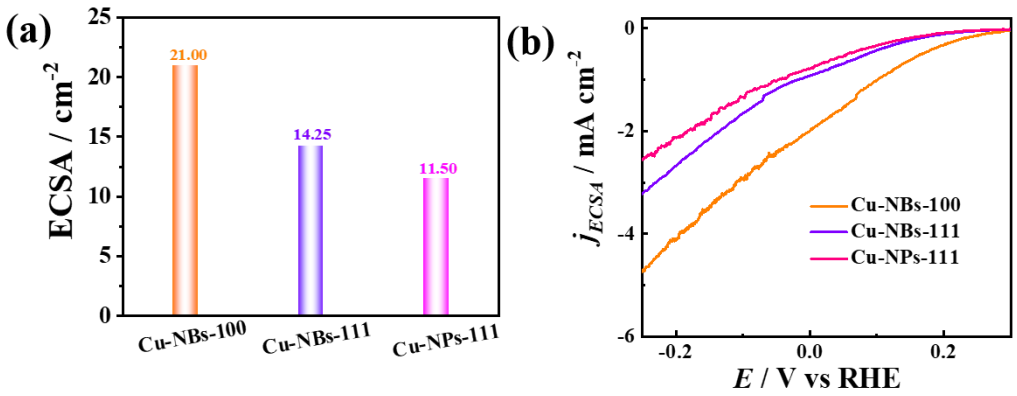

Figure S32 (a) Comparing ECSA values of Cu-NBs-100, Cu-NBs-111, and Cu-NPs-111. (b) LSV of above three electrocatalysts after normalizing ECSA in 1 M KOH with 0.1 M NO_3^-.

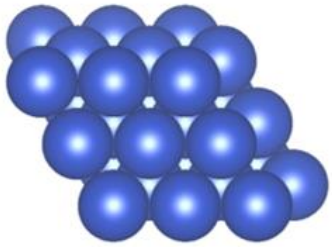

Figure S33 Structural model of Cu(111).

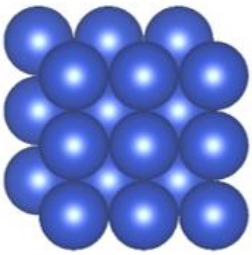

Figure S34 Structural model of Cu(100).

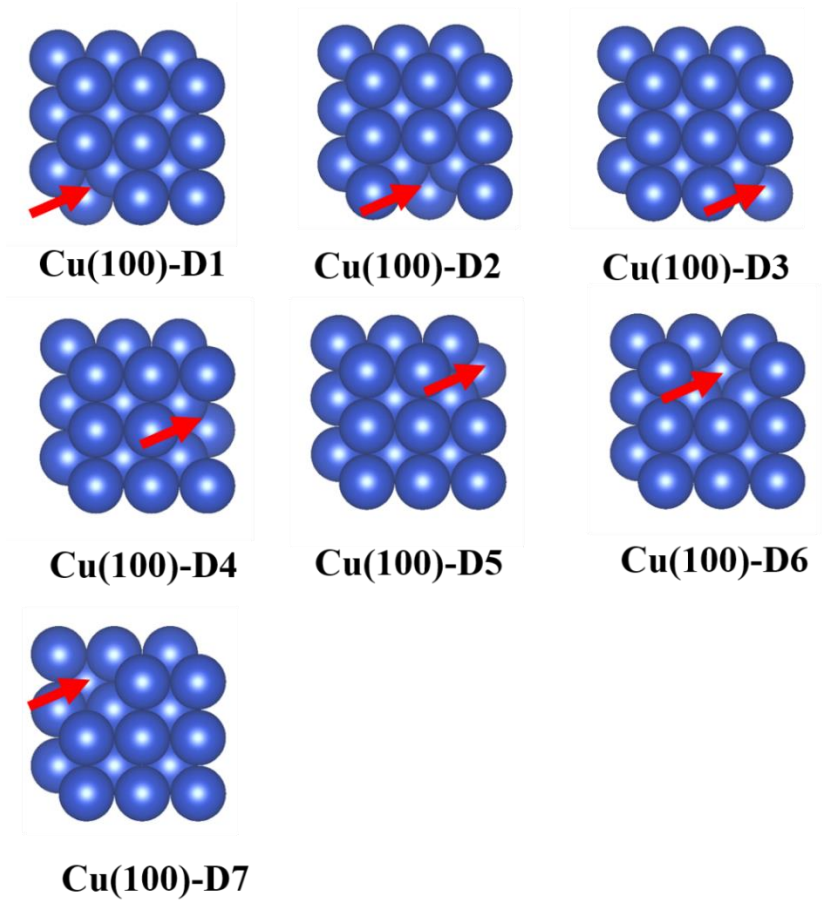

Figure S35 Structural models of Cu(100)-D with different locations of atomic defects, namely Cu(100)-D1, Cu(100)-D2, Cu(100)-D3, Cu(100)-D4, Cu(100)-D5, Cu(100)-D6, and Cu(100)-D7. (Locations of defects see the red arrows).

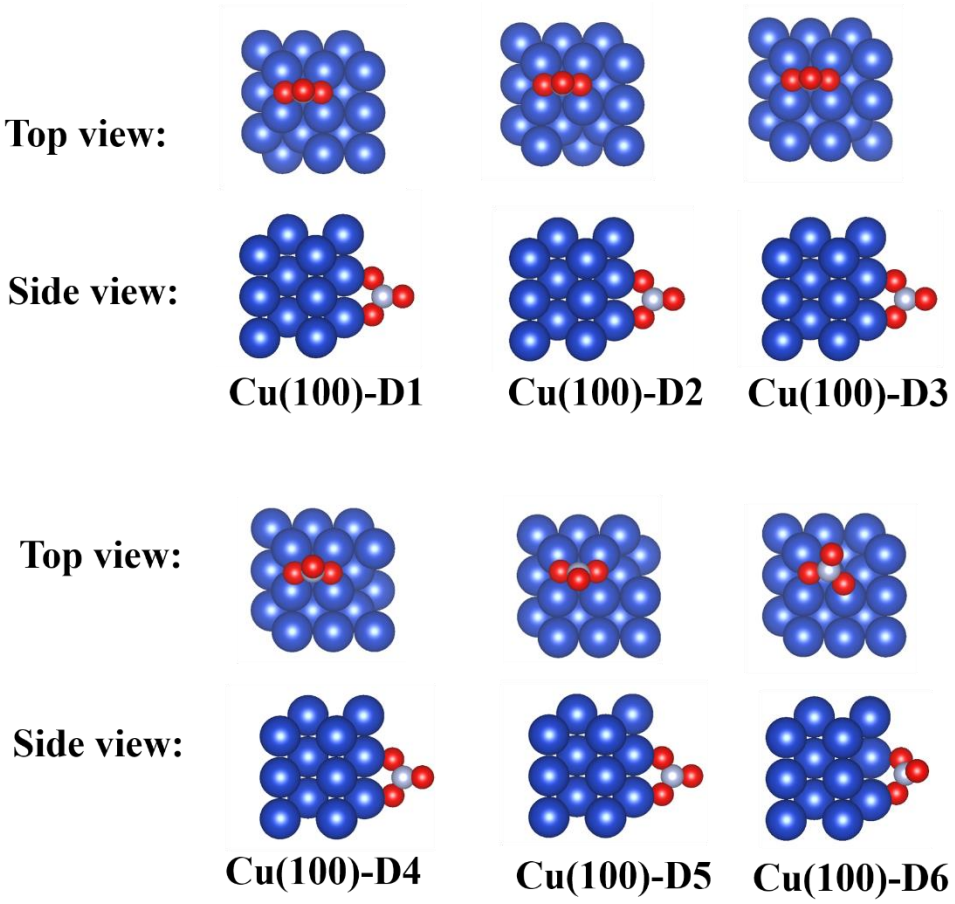

Figure S36 Optimized structural models of NO_3^- adsorbed on the Cu(100)-D1, Cu(100)-D2, Cu(100)-D3, Cu(100)-D4, Cu(100)-D5, and Cu(100)-D6. The blue, red, and white represent Cu, O, and N elements.

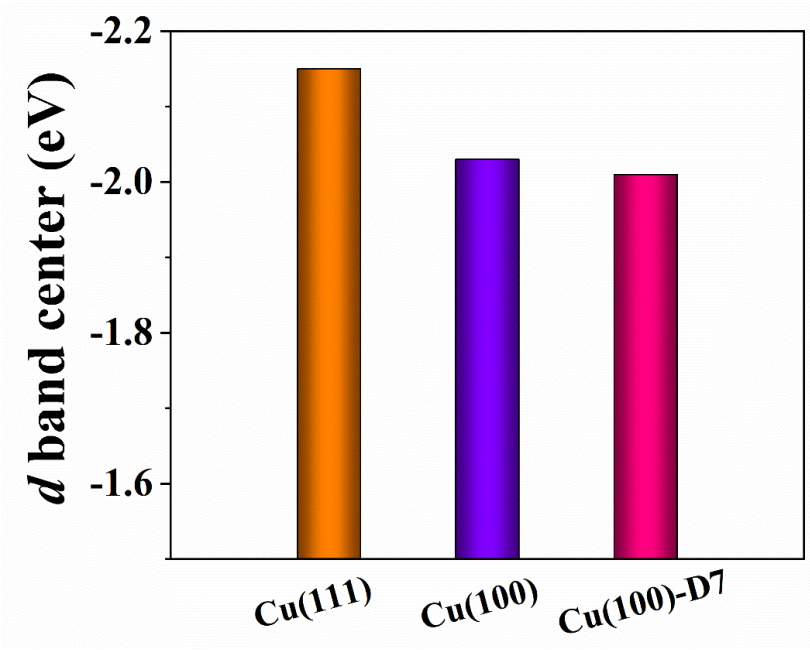

Figure S37 Comparing the *d* band center of Cu(111), Cu(100), and Cu(100)-D7 structural models.

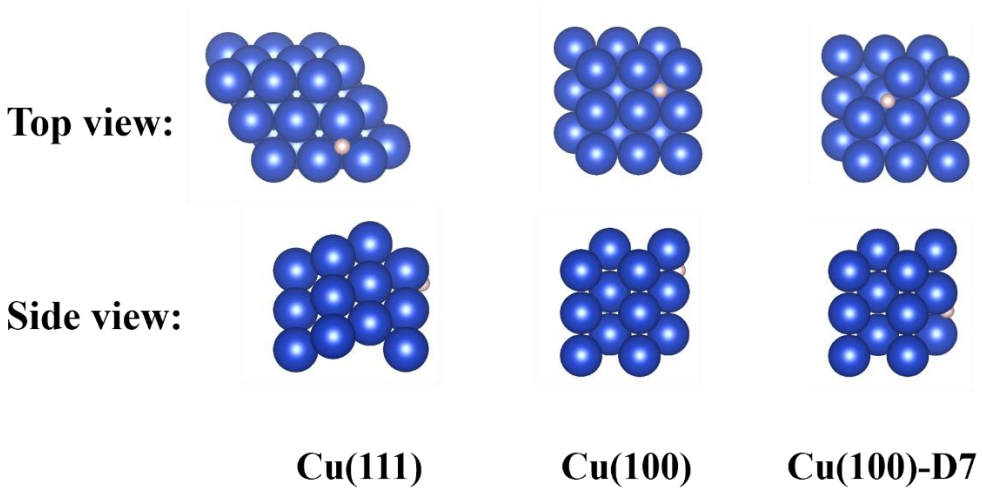

Figure S38 Optimized structures of H* intermediates adsorbed on the Cu(111), Cu(100), and Cu(100)-D7.

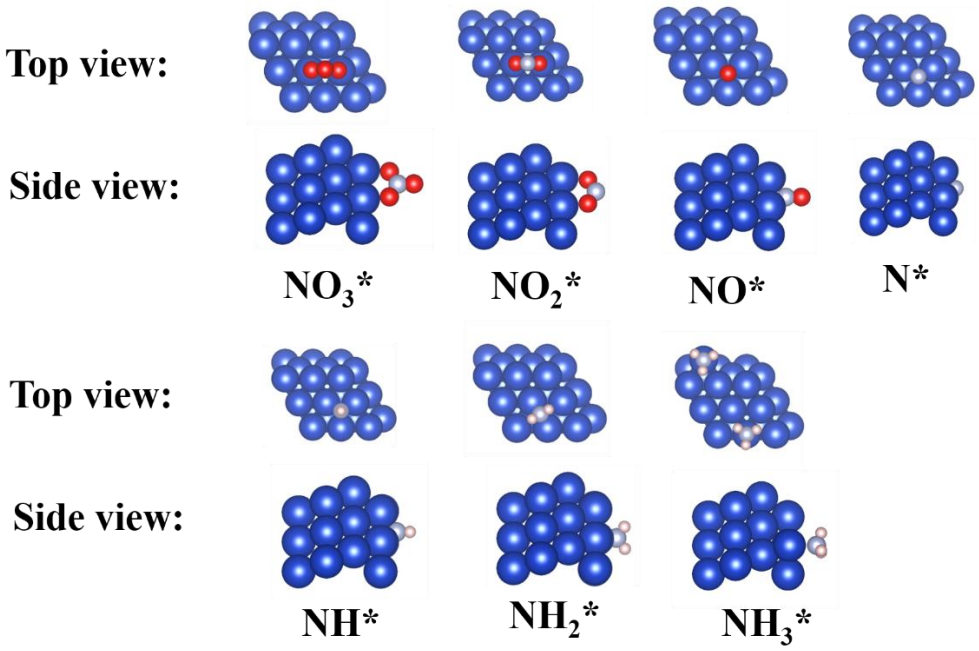

Figure S39 Optimized structures of all NO_3^-RR intermediates adsorbed on the Cu(111). The blue, red, and white represent Cu, O, and N elements.

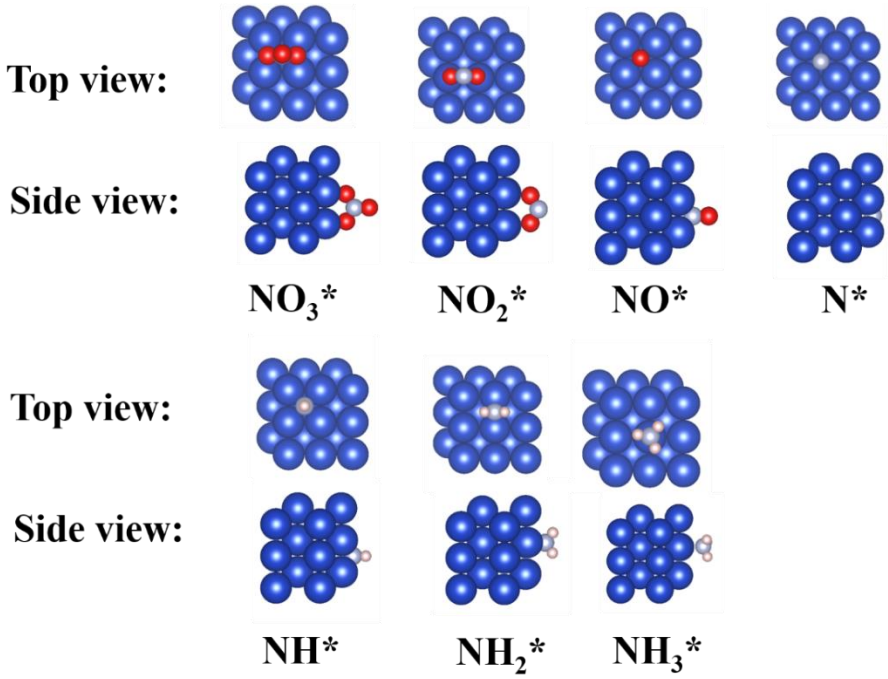

Figure S40 Optimized structures of all NO_3^-RR intermediates adsorbed on the Cu(100). The blue, red, and white represent Cu, O, and N elements.

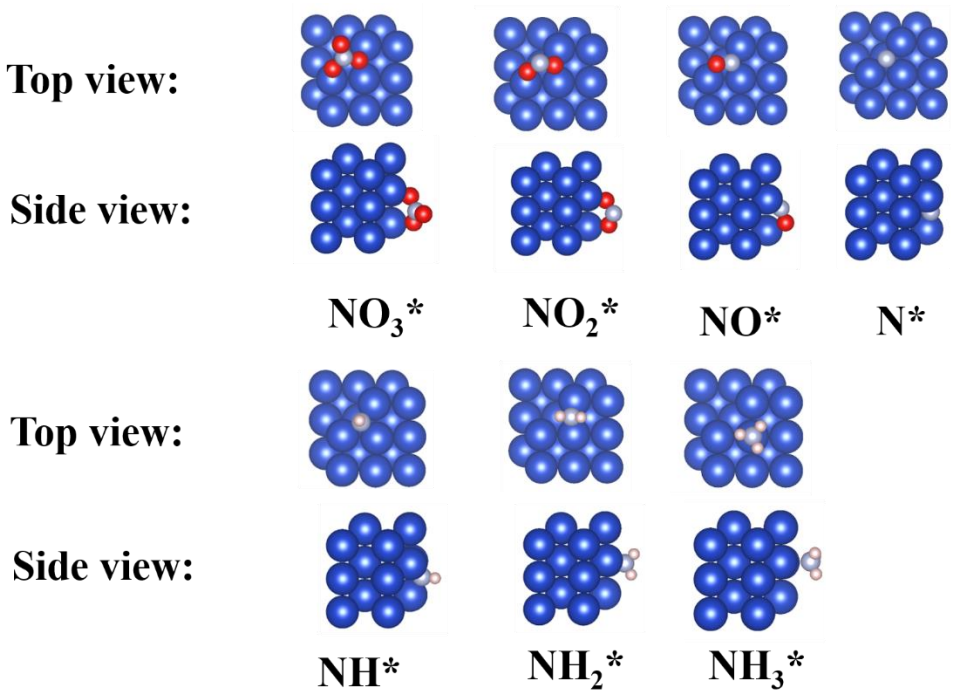

Figure S41 Optimized structures of all NO_3^-RR intermediates adsorbed on the Cu(100)-D7. The blue, red, and white represent Cu, O, and N elements.

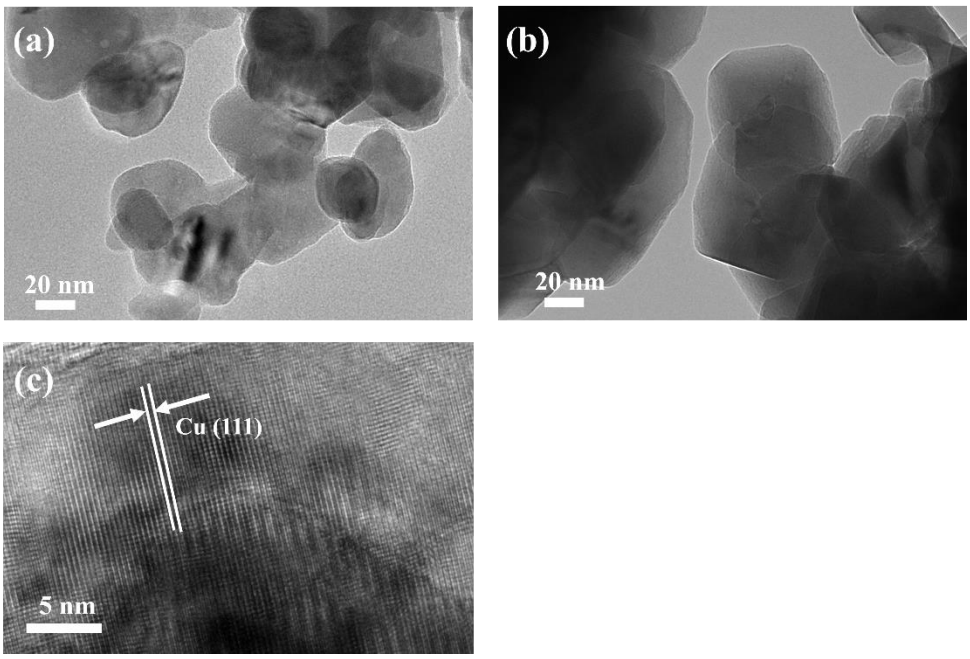

Figure S42 (a) TEM images of CuO NPs. (b) TEM and (c) HRTEM images CuO NPs after the electrochemical reduction at the potential of -0.4 V vs RHE in the electrolyte of 1 M KOH containing 0.5 M NO_3^-.

Table S1 Comparing the performance of our synthesized Cu-NBs-100 with other reported electrocatalysts for NO_3^-RR in alkaline media.

Electrocatalyst	Electrolyte	Potential (vs RHE)	NH_3 partial current density (mA cm^{-2})	NH_3 Selectivity	NH_3 yield rate	Ref.
Cu-NBs-100	**0.1 M KNO_3+1 M KOH**	**-0.15 V**	**288**	**95.3%**	**650 mol $g_{cat.}^{-1}$ h^{-1} (1.30 mmol cm^{-2} h^{-1})**	**This work**
Strained Ru Nanoclusters	1 M KNO_3+1 M KOH	-0.2 V	223.3	96 %	5560 mol $g_{cat.}^{-1}$ h^{-1} (1.17 mmol cm^{-2} h^{-1})	J. Am. Chem. Soc., 2020, 142, 7036-7046
Cu nanosheets	10 mM KNO_3+0.1 M KOH	-0.15 V	~7.5	99.7%	22.95 mol $g_{cat.}^{-1}$ h^{-1}	Appl. Mater. Today 2020, 19, 100620
Porous $Cu_{70}Ni_{30}$	0.1 M $NaNO_3$ +1 M NaOH	-0.276 V	~0.17	85.4 %	~4.121 mol $g_{cat.}^{-1}$ h^{-1} (~0.0026 mol cm^{-2} h^{-1})	Electrochim. Acta., 2014, 140, 337-344
Copper powders ($Cu_{6h, Air}$)	0.1 M $NaNO_3$+1 M NaOH	-0.376 V	~60	85 %	~0.2714 mol cm^{-2} h^{-1}	J. Electroanal. Chem., 2006, 596, 13-24
$Cu_{50}Ni_{50}$	0.1 M KNO_3+1 M KOH	-0.15 V	~53	~100%	N.A.	J. Am. Chem. Soc. 2020, 142, 5702–5708
NiAlMnCoCu alloy	0.25 M KNO_3+0.5 M KOH	-0.16 V	4.61	90%	N.A.	Electrochim. Acta 1999, 44, 2193−2197

Table S2 Comparing the performance of our synthesized Cu-NBs-100 with other reported electrocatalysts for NO_3^-RR in neutral media.

Electrocatalyst	**Electrolyte**	**Potential (vs RHE)**	**NH_3 partial current density (mA cm^{-2})**	**NH_3 Selectivity**	**NH_3 yield rate**	**Ref.**
Cu- NBs-100	**500 ppm KNO_3 + 0.1 M PBS**	**-0.6 V**	**40.8**	**72.88%**	**65.2 mmol $g_{cat.}^{-1}$ h^{-1} (0.131 mmol cm^{-2} h^{-1})**	**This work**
Cu–molecular	500 ppm NO_3^- + 0.1 M PBS	-0.4 V	17.2	85.9%	1.97 mmol $g_{cat.}^{-1}$ h^{-1} (0.026 mmol cm^{-2} h^{-1})	Nat. Energy., 2020, 5, 605–613
TiO_{2-x}	0.5 M Na_2SO_4 + 50-400 ppm $NaNO_3$	-0.744 V	~7.8	87.1%	45 mmol $g_{cat.}^{-1}$ h^{-1} (0.045 mmol cm^{-2} h^{-1})	ACS Catalysis, 2020, 10, 3533-3540
Co/CoO nanosheet	200 ppmNO_3^-+0.1 M Na_2SO_4	-0.444 V	~21.6	72%	~0.05 mmol cm^{-2} h^{-1}	Sci. China Chem, 2020, 63
Cu/Cu_2O NWAs	0.5 M Na_2SO_4 +200-2000 ppm $NaNO_3$	-0.3 V	< 17	N.A.	0.2449 mmol cm^{-2} h^{-1}	Angew. Chem., Int. Ed. 2020
Cu-Bi	100 ppm NO_3^- + 0.1 M Na_2SO_4	-0.944 V	6	19%	~0.0053 mmol cm^{-2} h^{-1}	J. Electroanal. Chem., 2018, 817, 202-209
Pd–Cu/γAl_2O_3	50 ppm NO_3^-	-0.844 V	10	19.6%	~0.0091 mmol cm^{-2} h^{-1}	Chem. Eng. J. 2016, 290, 201-208
Ti foil	0.4 M [NO_3^-] at pH ~0.77	-1 V	22	82%	N.A.	ACS Sustainable Chem. Eng. 2020, (10.1021/acssuschemeng.9b05983)
Co_3O_4/Ti	50 mg L^{-1} $NaNO_3$+0.05 M Na_2SO_4	N.A.	10	32%	N.A.	Water Res. 2017, 120, 1-11

Ni-Fe^0@ Fe_3O_4	50 ppm NO_3^- + 10 mM NaCl	N.A.	5	10.4%	N.A.	J. Clean. Prod. 2020, 242, 118569.
Co_3O_4-TiO_2-PVP	0.1 M Na_2SO_4, $NaNO_3$	N.A.	10	73%	N.A.	J. Environ. Chem. Eng. 2018, 6, 5249-5258

Reference

[1] A. A. Wei Zhe Teo, Martin Pumera *Electrochem. Commun.* **2013**, *28*, 51–53.

[2] Q. Hu, Z. Wang, X. Huang, Y. Qin, H. Yang, X. Ren, Q. Zhang, J. Liu, C. He, *Energy Environ. Sci.* **2020**,*13*, 5097-5103.

[3] D. Zhu, L. Zhang, R. E. Ruther, R. J. Hamers, *Nat. Mater.* **2013**, *12*, 836-841.

[4] L. C. Green, D. A. Wagner, J. Glogowski, P. L. Skipper, J. S. Wishnok, S. R. Tannenbaum, *Anal. Biochem.* **1982**, *126*, 131-138.

[5] G. Kresse, J. Furthmüller, *Phys. Rev. B* **1996**, *54*, 11169-11186.

[6] G. Kresse, D. Joubert, *Phys. Rev. B* **1999**, *59*, 1758-1775.

[7] J. Li, G. Zhan, J. Yang, F. Quan, C. Mao, Y. Liu, B. Wang, F. Lei, L. Li, A. W. M. Chan, L. Xu, Y. Shi, Y. Du, W. Hao, P. K. Wong, J. Wang, S.-X. Dou, L. Zhang, J. C. Yu, *J. Am. Chem. Soc.* **2020**, *142*, 7036-7046.

[8] J.-X. Liu, D. Richards, N. Singh, B. R. Goldsmith, *ACS Catal.* **2019**, *9*, 7052-7064.